Eur. Phys. J. D (2015) 69: 237
DOI: 10.1140/epjd/e2015-60204-7

THE EUROPEAN PHYSICAL JOURNAL D

Regular Article

Ion induced fragmentation cross-sections of DNA constituents*

Benedikt Rudek[a], Alexander Arndt, Daniel Bennett, Mingjie Wang, and Hans Rabus

Physikalisch-Technische Bundesanstalt, Bundesallee 100, 38116 Braunschweig

Received 30 March 2015 / Received in final form 13 July 2015
Published online 27 October 2015

Abstract. Proton collision with chemical analogs for the base, the sugar and the phosphor residue of the DNA, namely pyrimidine, tetrahydrofuran and trimethyl phosphate, respectively, has been investigated. The impact energies ranged from 300 keV up to 16 MeV. For the first time, relative fragmentation cross-sections for proton impact are reported for tetrahydrofuran and trimethyl phosphate; previously reported cross sections for pyrimidine are extended for energies beyond 2500 keV. Ionization of tetrahydrofuran leads to a ring break in about 80% of all events, trimethyl phosphate predominantly fragments by bond cleavage to one of the three methyl-groups and for pyrimidine the parent ion has the highest abundance. Such comparison supports earlier findings that the sugar is the weak spot for strand breaks.

1 Introduction

Ion-molecule interactions have been studied for many years. With the increasing use of proton and carbon ions in cancer treatment, interaction of ions with molecules from biological tissue was shifted into focus [1–5]. In these radiotherapy modalities, treatment planning is not only based on the conventional dosimetric quantity, namely, the absorbed dose to water. An additional weighting factor is employed to account for the enhanced relative biological effectiveness (RBE) of ions compared to high-energy photons. RBE is related to the particle track structure, i.e. the microscopic spatial distribution of ionizations and energy transfers. The European project "Biologically weighted quantities in radiotherapy (BioQuaRT)" [6] aims at developing measurement and simulation techniques for determining the physical properties of ionizing particle track structure on different length scales. By using the newly developed track structure simulation tool and the outcomes of dedicated radiobiological experiments on an ion microbeam, it investigates up to the cellular level how these track structure characteristics correlate with the biological effects of radiation. In the scope of this simulation tool, fragmentation cross sections of DNA constituents are used as they not only give a measure of the ionization probability but also indicate whether the ionization leads to a strand break and what kind of radicals are created.

To investigate DNA constituents, small molecules with structural similarities, that can easily be put into the gas-phase without decomposition, were chosen. As chemical analogs for the base, the sugar and the phosphor residue of the DNA pyrimidine, tetrahydrofuran (THF) and trimethyl phosphate (TMP), respectively, were used (Fig. 1).

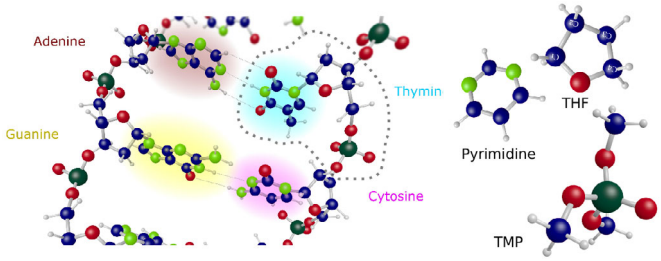

Fig. 1. Sketch of a segment of the DNA with the four bases highlighted [7]. On the right side, the three investigated chemical analogs are arranged in the same manner for comparison.

Pyrimidine ($C_4H_4N_2$) is an aromatic heterocyclic organic compound, containing four carbon atoms and two nitrogen atoms at positions 1 and 3 in the ring. The molecule is the building block of three types of nucleobases: cytosine, thymine, and uracil.

Tetrahydrofuran ($(CH_2)_4O$) is a cyclic ether with one oxygen atom and four (CH_2) molecules in the five-membered ring. The ring is a constituent of deoxyribose in furanose form. In nucleotides, it provides bonds to the phosphate groups and a nucleobase at C(3) and C(4), and C(1), respectively. Bond breaks at deoxyribose were found to be a key intermediate in producing strand breaks, which are the most severe form of lesion in radiation damage to DNA [8,9].

Trimethyl phosphate ($C_3H_9PO_4$) is the trimethyl ester of phosphoric acid with the hydrogen atoms replaced by methyl groups. Similarly, the phosphate group in the DNA

* Contribution to the Topical Issue "COST Action Nano-IBCT: Nano-scale Processes Behind Ion-Beam Cancer Therapy", edited by Andrey Solov'yov, Nigel Mason, Gustavo García, Eugene Surdutovich.

[a] e-mail: benedikt.rudek@ptb.de

forms phosphodiester bonds to the aforementioned carbon atoms in the deoxyribose of two neighboring nucleotides to build up the DNA backbone.

In this work, relative fragmentation cross sections for proton impact energies from 300 keV up to 16 MeV are presented. Measurements in the Bragg peak region, i.e. proton energies around 100 keV for tissue-equivalent material, have recently accomplished and will be discussed in a subsequent paper. Experiments on larger building blocks of the DNA are planned. After parametrization, the cross sections will be used in the GEANT4-DNA simulation tool [10].

The paper is structured as follows. In Section 2 the experimental procedure and data analysis is described. Section 3 presents results. Finally, in Section 4, the conclusions are drawn.

2 Experimental procedure

The experimental setup was built by A. Arndt to study fragmentation cross-sections of small bio-molecules by electron impact. For the presented measurements, it was then adapted for the use with ion beams.

2.1 Sample injection

The gas target was introduced into the interaction zone by means of a supersonic gas-jet. It provides a dense, well localized, and internally cold gas target. The upper part of Figure 2 shows a sketch of the reservoir, nozzle and skimmer. Following the design used for momentum spectroscopy [11], the target gas at pressures of up to 10 bar (here, about 2 bar) expands through a gas nozzle with 30 μm diameter into a vacuum chamber, which is equipped with turbomolecular pumps of high pumping speed to achieve pressures of 10^{-3} mbar at load. In the ideal case of an adiabatic isochore expansion of an ideal gas, the internal energy and the compressional energy are converted to kinetic energy of the gas atoms, which are, thus, reaching a supersonic speed. In practice, the region of supersonic flow is limited to the so called "zone of silence" downstream of the nozzle. A conically formed aperture (called "skimmer") of 200 μm diameter, is placed inside the zone so that only the dense, internally cold part of the gas jet is entering the high-vacuum experimental chamber.

To investigate liquid samples, a manifold for mixing the liquid and a seeding gas (helium) was designed. The gas pressure of the seeding gas was used to push the liquid into a reservoir mounted in front of the nozzle. Because pyrimidine and trimethyl phosphate reacted with the cupreous reservoir, a gold coating was galvanically added. The seeding gas had separate lines into the reservoir, so that the liquid level and pressure could be controlled. To increase the vapor pressure of the liquid and avoid clustering, the reservoir was heated to 140 °C for THF and 180 °C for pyrimidine.

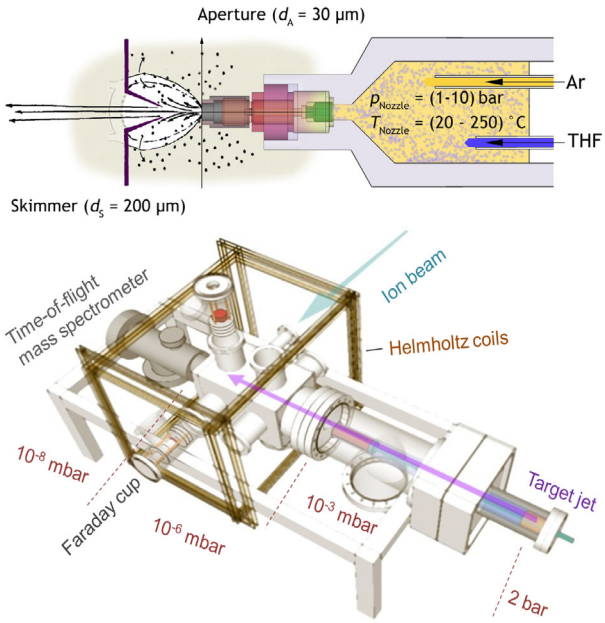

Fig. 2. Above: sketch of the heatable target mixing reservoir, gas nozzle and jet skimmer. Below: drawing of the crossed-beam experiment indicating the gas pressure in the nozzle and vacuum conditions in the expansion-, the interaction- and the spectrometer-chamber. The ion beam current was measured in the Faraday cup, fragment cations were detected in the time-of-flight mass spectrometer.

For the initial experiments, an electron gun was mounted as close as possible to the interaction zone. A dense and well localized gas jet was needed for the spectrometer, while at the same time a high vacuum environment was required for the stable operation of the electron beam. For the ion beam experiments, the vacuum requirements were less. In fact, in the second week of beamtime the supersonic jet was unusable when the skimmer got loose after an accidental venting, so that the experimental chamber had to be flooded with the target gas (TMP) to finish the measurements.

The lower part of Figure 2 displays a CAD drawing of the crossed-beam experiment indicating the vacuum conditions along the target jet. The Helmholtz coils were required for active suppression of the earth magnetic field during electron beam experiments but have not been used for the ion beam measurements.

2.2 Ion detection

A commercial time-of-flight mass spectrometer in reflectron design was used (Mini-TOF-MS by Kore Technologies, Ltd.). It extracts the fragment ions from the interaction volume with a voltage pulse of –350 V through a 4 mm entrance aperture. The spectrometer chamber is separately pumped to guarantee a high-vacuum environment for the detector (between 10^{-8} mbar and 10^{-6} mbar) when the experimental chamber is operated with sample gas (between 10^{-6} mbar and 10^{-4} mbar). The fragment

ions are focused by an electrostatic lens, accelerated to −2 kV and deflected into an array of electrodes, where the applied voltage increases from –2 kV to 0 V to reflect the ions towards the detector. The ion detector is a discrete dynode electron multiplier detector (ETP AF824 by Scientific Instrument Services, Inc.).

The ion optics can be adjusted for focusing a extended interaction zone. A SimIon8 [12] ion-trajectory simulation with ion-beam size and spectrometer parameters as used in the experiment showed that the area seen by the detector was of maximum 3 mm in diameter parallel to the entrance aperture. This area is lager than the estimated 1 mm size of the supersonic gas jet in the interaction zone, but in the case of the TMP-flooded chamber the interaction zone is larger and extending along the whole primary ion beam. The simulation also confirmed that the position of the primary ion beam relates to a time-of-flight offset and its width to the peak-width of all masses in the time-of-flight spectrum.

The reflectron design focuses ions of different kinetic energy onto the detector which increases the time-of-flight resolution. For kinetic energies above two times the thermal energy (2×25 meV), the transmission is reduced, which is a common behavior for this kind of spectrometer design [13]. For ion-neutral fragmentation, the kinetic energy release usually is in the range of only 1 meV to 50 meV [14]. An (e, 2e + ion) study on THF in particular found maximum KERs below 50 meV for all fragments. At such energies, the transmission for hydrogen was simulated to be 20% due to its high velocity even at low kinetic energies, but starting from 20 amu the transmission is close to 100% for fragments originating from ion-neutral fragmentation. Higher kinetic energies occur in Coulomb explosions upon multiple ionization. In ion-molecule collisions multiple ionization is enhanced by charge transfer processes. E.g., for collision of alpha particles with amino acids [15] or carbon ions with thymine [16], kinetic energies in the order of 5 eV were found and the energy was increasing with the charge state of the carbon projectile. While charge transfer plays an important role in ionization by carbon ions [17], it was experimentally found to have little impact for the ionization by protons [18]. Recent theoretical work quantifies that the charge transfer cross section for pyrimidine nucleobases in collisions of C^{4+} is four orders of magnitude higher than in collisions with protons (controversially, it would be lower in the case of deoxyribose) [19]. Regarding an estimate of Coulomb explosions, single ionization was reported to be 50 times more likely than double ionization for a 100 keV proton beam impacting on H_2O [20]. Thus, we do not expect significant contributions from high-KER Coulomb explosions in our proton beam experiment and we assume the spectrometer transmission to be constant for all relevant fragments.

The signal of the electron multiplier is decoupled in a comparator circuit and digitized by a discriminator within the pre-amplifier. In this ion-counting mode, mass-dependent amplification stemming from velocity-dependent detector signal amplitudes is suppressed. Finally, the time-of-flight spectrum is obtained from a 4 GHz time-to-digital converter. This corresponds to a 0.25 ns time resolution.

The peak-width in a time-of-flight spectrum changes with the m/q ratio. To compare fragments for different proton energies, the integration interval was adjusted for peaks of varying m/q ratio. For TMP, a group of six neighboring mass peaks was integrated. Because the ion beam was not pulsed, a small number of ion-fragments was created during the 2 μs extraction pulse of the spectrometer, which resulted in a horizontal tail behind large mass peaks. For subsequent mass peaks, this tail was equal to a baseline shift, which was subtracted for each mass peak.

2.3 Ion beam

The experiment was carried out at beamline two of the PTB ion accelerator facility [21]. Two different kinds of accelerators are available, namely, a Van de Graaff accelerator with voltages between 0.3 MeV and 3.74 MeV, and an energy-variable cyclotron providing ion beams with energies up to 27 MeV. Ion energies between 0.3 MeV and 3 MeV have been measured using the Van de Graaff accelerator, data for 9.5 MeV and 16 MeV ions were taken using the cyclotron. The accuracy of the ion energy is ±1 keV for the Van de Graaff accelerator [22] and ±15 keV for the cyclotron.

The beamline and the experimental chamber were separated by a differential pumping stage to prevent leakage of target gas into the ultra high vacuum of the beamline. Additionally, a sequence of three isolated tantalum apertures with diameters of 5 mm, 3 mm and 5 mm and a separation of 10 mm were mounted inside. The inner aperture was connected to an electrometer to read the current of the incident ion beam and the outer, larger apertures were biased to –300 V to suppress electron emission from impact ionization, which lead to an overestimation of the measured ion current. The ion optics were adjusted maximizing the ion current in a Faraday cup mounted downstream of the experimental chamber while minimizing the ion current at the aperture. At energies lower than 1 MeV the available focusing optics are less effective and the ion beam becomes wider, which was observed in the current ratio from Faraday cup and aperture. A beam profile monitor was not used at that time so that a more detailed characterization is unavailable. We can, however, get a rough estimate of the beam width from the pulse shape of the time-of-flight peaks (see Sect. 3.2). After the beamtime the pulse-width and shape was compared to the standard values and several mass spectra at low energies had to be disregarded. The Bragg peak energies around 100 keV, that were measured with a different accelerator, will be discussed in a follow-up paper.

For the first measurement, a 420 keV proton beam on tetrahydrofuran, the beam current was limited to 100 nA, afterward it was increased to about 500 nA for all measurements with the Van de Graaff accelerator. The cyclotron delivered about 150 nA for proton beams.

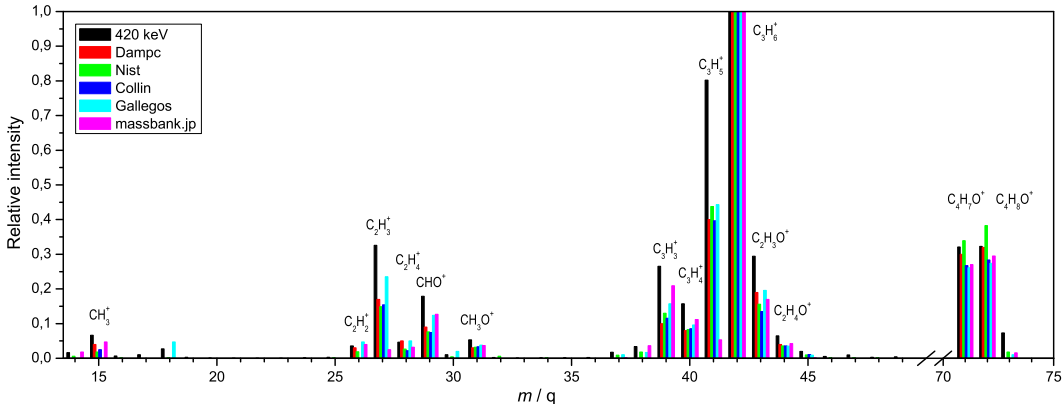

Fig. 3. Mass spectrum of tetrahydrofuran in percentage ratio to the most intense mass of 42 amu. Data for 420 keV proton energy are compared with electron impact mass spectra by Gallegos (70 eV) [23], Collin (50 eV) [24], Dampc (140 eV) [25], the massbank.jp [26] and NIST [27].

3 Results and discussion

3.1 Tetrahydrofuran

Ionization due to proton collision leads to the THF parent $C_4H_8O^+$ cation and formation of cation fragments. The mass spectrum of THF cations for 420 keV proton impact together with assignments of the mass peaks in percentage ratio to the most intense mass of 42 amu is displayed Figure 3. The relative fragmentation cross sections are shown in Figure 4 for energies of 420 keV and 9.5 MeV. The cross sections are normalized to the sum of all displayed fragments. For clarity, only the most abundant fragments are displayed.

Four distinct groups occur in the mass spectrum: in the mass ranges 14–18 amu, 26–32 amu, 36–48 amu and around 72 amu. Masses in the range 46–62 amu have been reported for electron impact with low abundance below 0.6% relative intensities [25] which are not resolved here. To emphasize the main fragments, the following cations are not displayed in Figure 3: the hydrogen (1 amu) peak is suppressed due to poor transmission of fast light ions; a peak at 4 amu stems from the helium carrier gas, peaks larger than 73 amu from small pyrimidine or TMP contamination.

Clustering is well known to appear in supersonic gas jets, when the gas target is cooled down by the expansion and interaction with the carrier gas [28]. The dimer at 144 amu, is the most abundant cluster of THF at common parameters [29]. The supersonic gas jet used by Ren is very similar to ours, but run at room temperature whereas we heated the THF reservoir to 140 °C. The extended mass spectrum of Ren's publication [30] indeed shows a 5% contribution around 144 amu, but in our mass spectra we could not find any dimer. Note, that we are comparing mass spectra of low-energy electron-impact and high-energy proton-impact, so that not all differences are due to cluster formation. A general feature, however, can be attributed to the dissociation of the dimer: with the 5% cluster contribution the mass group around the parent ion (72 amu) is about one third higher and the

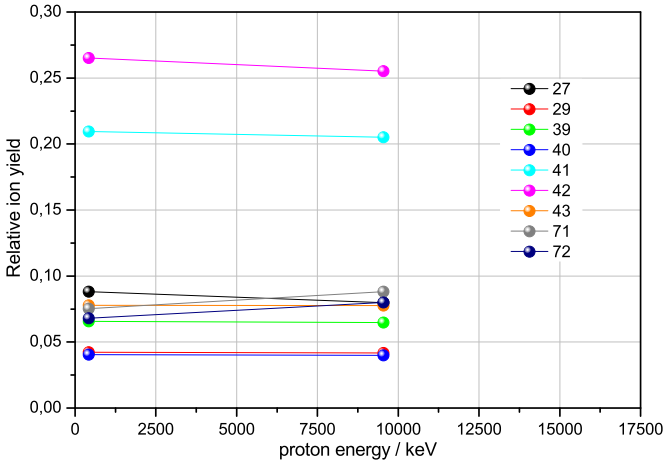

Fig. 4. Relative fragmentation cross section of the most abundant tetrahydrofuran fragments versus proton beam energy. The cross sections are normalized to the sum of all displayed fragments.

mass group around the main fragment (42 amu) about one third lower than in our spectra. Apparently, dissociative ionization of the dimer will most likely yield a parent ion or the 114 amu fragment (the dimer minus the 30 amu fragment of the main dissociation channel). Dissociative ionization of the monomer, however, will most likely yield the main fragment (42 amu). The dominating fragment has a mass of 42 amu, followed by the 41 amu fragment. Mass 42 amu can appear in two different dissociation channels. Cleavage of the O-C(4) and C(1)-C(2) bonds leads to the fragments cyclopropane $C_3H_6^+$ (42 amu) and formaldehyde CH_2O (30 amu), cleavage of the C(1)-C(2) and C(3)-C(4) bonds to ethenone $C_2H_2O^+$ (42 amu) and ethane C_2H_6 (30 amu). In an electron impact experiment with variable delays between ionization and ion extraction we previously found that the dissociation channels can be distinguished by the kinetic energy release (unpublished, paper in preparation). Kinetic energies of different mass peaks have been discussed by Ren [30] but

competing dissociation channels hidden in one mass peak are not resolved in their work. From calculation of the standard enthalpy of formation, Collin attributes mass 42 to $C_3H_6^+$ [24], after Gallegos found $C_2H_2O^+$ to be more likely [23]. More recently, Scala argues that cyclic ethers predominantly react via breakage of the C-O σ-bond forming an intermediate oxy-tetramethylene diradical which then further decomposes by cleavage processes involving the C-H and C-C bonds [31]. Accordingly, mass 42 is attributed to $C_3H_6^+$ rather than $C_2H_2O^+$. In case of hydrogen migration to the neutral fragmentation partner or subsequent hydrogen loss, mass 41 amu, 40 amu or 39 amu will be detected. If hydrogen atoms migrate from the 30 amu fragments before the breakup, mass 43 amu and 44 amu can be detected. Further fragmentation of the neutral fragments, such as the formation of CO and H_2 from CH_2O cannot be excluded. About 60% of all ion fragments belong to the group between mass 39 amu and 44 amu. Its dissociation partner (26 amu to 31 amu) carries the charge much less often and is found in 15% of all ionizing events.

The parent $C_4H_8O^+$ ion has mass 72 amu and 71 amu after hydrogen loss. Both result from ionization of the highest occupied molecular orbital (HOMO) of THF, while ionization of lower lying orbitals will lead to fragmentation and, thus, lighter fragments [30]. Because the ratio of the ionization cross sections for the HOMO and the total ionization cross section is almost constant over the measured projectile energy range, a constant yield of 72 amu and 71 amu over the energy range is expected.

Recently, Wasowicz presented luminescence spectra for excited neutral THF fragments after H^+, C^+, and O^+ collisions [32]. Apart from this study, no data were reported previously on cationic interactions with THF. Thus, we compare our data to spectra for electron collisions with electron impact above all appearance energies. The most notable discrepancy among mass spectra for electron collisions was the appearance of mass peak around 55 amu, that was reported by Fuss [33] and Ren [30], but could not be observed by Gallegos [23], Collin [24], Dampc [25], the massbank.jp [26] and NIST [27]. The formation of that mass peak requires the simultaneous breakage of two C-O bonds, which is energetically unfavorable [31]. Because electron-energy, spectrometer transmission or cation lifetime cannot explain the discrepancy among mass spectra, we attribute it to contamination or strong clustering in the gas target. In Figure 3, mass spectra for proton energies of 420 keV are compared to the literature excluding Fuss [33] and Ren [30]. The mass peak at 42 amu is normalized to 100% in all spectra. The mass spectra for electron and for ion collisions are generally in good agreement. For 420 keV proton impact, corresponding to about 4 Bohr velocities, more intense fragmentation and hydrogen migration is observed compared to electron impact. For pyrimidine, it was discussed that the energy transferred to some deeper molecular orbitals decreases with the electron energy while it increases for protons, that have their cross section maximum at lower energies (at about 100 keV) [34]. Charge transfer would lead to even stronger fragmentation for multiple charged cation projectiles [16], but for singly charged ions, especially for protons, the charge transfer cross section is low [18,35].

A recent theoretical study on deoxyribose ($C_5H_{10}O_4$) in the furanose conformation has shown that the first fragmentation step involves the breaking of the C-O bond in the ring but also breaking of the CH_2OH chain [9]. Experimental work confirm that the most abundant fragments are grouped around the oxygen and the carbon monoxide peak due to the break up between such hydroxyl or carbonyl groups and the ring [36]. The next most abundant fragment has mass 42 amu, which is attributed to cleavage of the furanose ring indicating that the same dissociation processes appear as for THF. Thus, it sould be noted that the model analog THF is limited to describe the fragmentation of the deoxyribose ring.

3.2 Pyrimidine

The mass spectrum of the pyrimidine parent and fragment cations for 1.55 MeV proton impact together with assignments of the mass peaks in percentage ratio to the most intense mass of 80 amu is displayed in Figure 5. The data is compared to references [27,37,38]. In order to allow comparison to data by Wolff [34] the mass peak 79 amu from hydrogen loss and the isotopic mass peak 81 amu are added to the mass peak at 80 amu. The relative fragmentation cross sections are shown in Figure 6 for energies between 300 keV and 16.1 MeV. Between 125 keV and 2.5 MeV, fragmentation data for proton impact by Wolff [34] are added to the graph. The cross sections are normalized to the sum of all displayed fragments. As in Wolff et al., only the most abundant fragments are displayed. For the two highest energies, which were taken at the very end of the measurement campaign, a contamination of pyrimidine with THF (approximately 10%) and vice versa was observed. For pyrimidine, the THF spectrum was scaled to the contaminating THF parent-ion peak in the pyrimidine spectrum and then subtracted from that spectrum; for THF vice versa. Given that no chemical reaction took place, the contamination can be neglected as there are only few common fragments of small yield for pyrimidine and THF.

The mass spectrum in Figure 5 shows distinct groups corresponding to the number of carbon and nitrogen atoms withing the fragment cation. The non-fragmented ring $C_4H_4N_2^+$ at 80 amu dominates the spectrum. The loss of one carbon or nitrogen atom would result in a mass group around 68 amu. As in previously reported studies on electron- [38–40], proton- [34] and photon-induced fragmentation [37,41], this group was absent in our spectra.

The lighter fragment ions build a group around 53 amu ($C_3H_3N^+$), which is formed when the parent ion looses a HCN molecule. The loss of HCN moieties, which is thermodynamic stable, was reported to be a general feature in fragmentation processes of nitrogen heterocycles [37,42]. Mass 54 amu is assigned to the HCN fragment including the ^{13}C or ^{15}N isotope. Our data show a higher ratio than expected from the combined 3.9% isotopic abundance, probably because the contribution from the tail

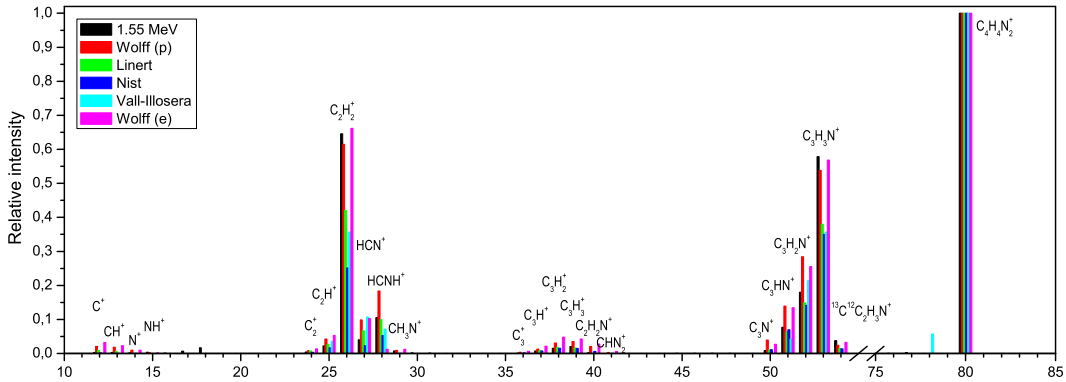

Fig. 5. Mass spectrum of pyrimidine in percentage ratio to the most intense mass of 80 amu. Data for proton energy of 1.55 MeV are compared with the proton impact mass spectrum of Wolff (1.5 MeV) [34], the electron impact mass spectra of Linert (140 eV) [38], NIST [27] and of Wolff (400 eV) [34], and the photo-fragmentation mass spectrum of Vall-llosera (15.7 eV) [37].

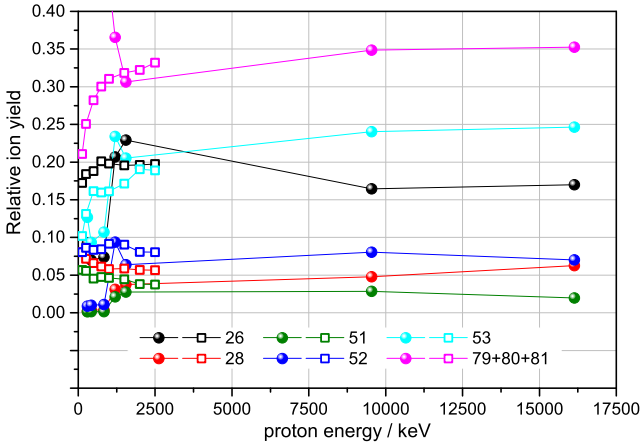

Fig. 6. Relative fragmentation cross section of the most abundant pyrimidine fragments versus proton beam energy. The cross sections are normalized to the sum of all displayed fragments. Data points marked by squares are taken from Wolff [34].

of the 53 amu peak was not fully subtracted. The three lighter cations, 50, 51 and 52 amu form via hydrogen loss.

The mass peak at 39 amu is about an order of magnitude smaller than for THF. For THF, it was assigned to $C_3H_3^+$ following hydrogen loss from the dominating fragment $C_3H_6^+$. For pyrimidine, $C_3H_3^+$ can be created by breakup of the two C-N bonds. The breakup of one C-N and one C-C bond could also lead to a cation of 39 amu (C_2HN^+), but was calculated to be energetically less favourable [37].

The second most abundant cation is found at mass 26 amu. After $C_3H_3N^+$ (53 amu) is formed by HCN loss, an additional HCN loss will form the acetylene cation $C_2H_2^+$ (26 amu) [42]. The 27 amu peak can be either assigned to protonated acetylene $C_2H_3^+$ or HCN^+ stemming from the main breakup channel. If hydrogen migration onto this fragment occurs during the dissociation, the $C_2H_4^+$ or $HCNH^+$ (28 amu) is formed.

The abundance of the carbon ion, C^+ (12 amu) and CH^+ (13 amu), is even lower than in literature, possibly due to reduced spectrometer transmission for fast light ions. The mass peak at 18 amu is due to water contamination in the hygroscopic pyrimidine.

In Figure 5, mass spectra for low energy electron-impact (estimated 70 eV for NIST [27] and 140 eV for Linnert [38], corresponding to a velocity of about $3v_{\mathrm{Bohr}}$), for photon-induced fragmentation (15.7 eV [37]) and proton-impact (1.5 MeV [34], about $7.5v_{\mathrm{Bohr}}$) are compared. In comparison to the standard energies in electron-driven mass spectrometer, ion impact leads to a higher ratio of the fragment cations. However, compared to higher electron energies (400 eV, i.e. about $5.5v_{\mathrm{Bohr}}$ [34]), the fragmentation pattern becomes very similar. Thus, our proton data confirms the findings by Wolff, that for impact velocities below $5v_{\mathrm{Bohr}}$ the dissociation cross section for proton impact is larger than for electron impact.

The fragmentation cross sections vs. proton energy (Fig. 6), cuts off a 80% ratio for the parent ion (80 amu) for the proton energies of 300 keV, 420 keV and 840 keV. We found a similar extreme ratio in reference [26], but this is probably due to averaging of spectra below and above the appearance energies. We realize that the peak width in those three spectra doubles indicating an inproper focusing of the proton beam. A wide ion beam increases the interaction zone and the transmission for ionic fragments decreases outside the spectrometer acceptance volume.

For energies from 1.5 MeV to 16.1 MeV, the relative cross sections from our measurements are extending those reported by Wolff up to 2.5 MeV. At those energies, the parent ion has a yield of 35% and is the most abundant fragment, which is in contrast to THF, where the parent ion has a yield of less than 10%. In a previous work by Deng on desorption mass spectra of the base thymine, the deoxyribose and the nucleoside thymidine it was found that most fragments of thymidine, which combines thymine and the deoxyribose, originate from the sugar moiety [44]. Apparently, the sugar backbone is more fragile than the nucleic acid base, which aligns very well to our findings for the chemical analogs THF and pyrimidine.

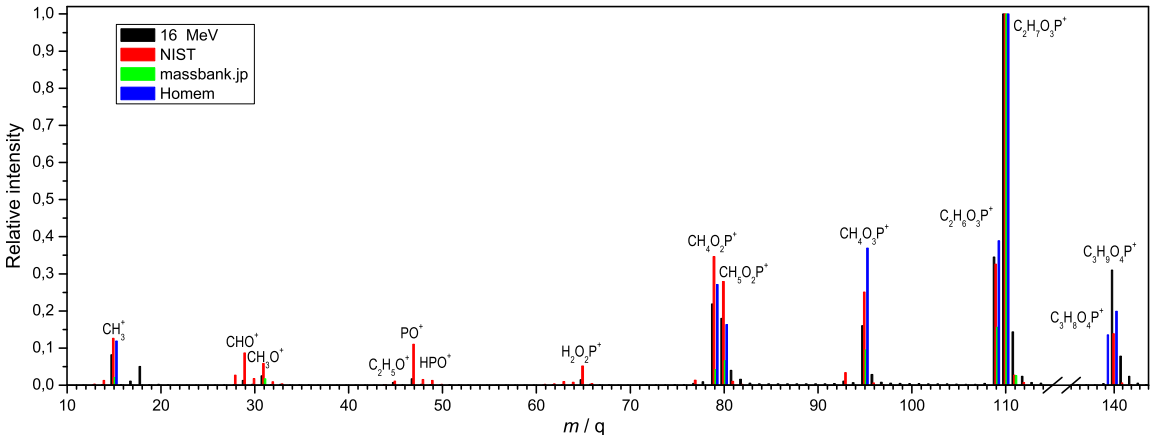

Fig. 7. Mass spectrum of trimethyl phosphate in percentage ratio to the most intense mass of 110 amu. Data for proton energy of 16 MeV are compared with the electron impact mass spectra of massbank.jp [26] and NIST [27], and the photo-fragmentation mass spectrum of Homem (21.35 eV) [43].

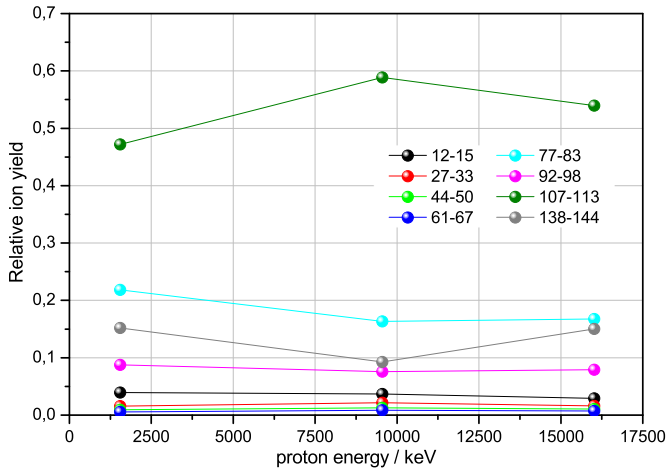

Fig. 8. Relative fragmentation cross section of the most abundant trimethyl phosphate fragments versus proton beam energy. The cross sections are normalized to the sum of all displayed fragments.

3.3 Trimethyl phosphate

The mass spectrum of the TMP in percentage ratio to the most intense mass of 110 amu for 16 MeV proton impact together with assignments of the mass peaks is displayed in Figure 7. The data is compared to literature [26,27,43]. The relative fragmentation cross sections are shown in Figure 8 for proton energies between 1.55 MeV and 16 MeV. Because for masses above 80 amu individual mass peaks could not be resolved for energies other than 16 MeV, the fragments are displayed in groups of six neighboring masses.

The non-fragmented TMP ($C_3H_9O_4P^+$) lies at 140 amu. Additionally to the parent ion, seven groups of fragment cations are observed. The mass peaks around 110 amu are dominating the spectrum with a combined 60% abundance of all cations. The next lighter fragments, around 95 amu and around 79 amu, contribute less then 10% and 20%, respectively. Yields for cations around 65 amu, 47 amu and 31 amu are very low and not included in the data for 21.35 eV photon impact [43] and for electron impact by massbank.jp [26]. Mass 15 amu is found in all data sets. Bafus reports extremely high yields for lighter cations [45]. Because we believe this is an artifact of mass-dependent detector efficiency and analog read-out [46] we exclude his data in our comparison in Figure 7.

While competing dissociation channels describe the fragmentation of the heterocyclic molecules THF and pyrimidine, sequential emission of formaldehyde (CH_2O) or a methoxy radical (OCH_3) govern the fragmentation of TMP. Photoelectron spectra show an initial electron emission from a σ_{CH} bond which is followed by a hydrogen migration from the methyl-group to the non-methylated oxygen [43]. Such keto-enol isomerization is common for phosphorus esters [47]. As a consequence of the induced charge rearrangement, formaldehyde (CH_2O) is dissociating and $C_2H_7O_3P^+$, the largest mass peak at 110 amu, is formed. Mass 109 amu is formed when the σ_{POCH} orbital is ionized and the methoxy radical (OCH_3) dissociated without previous isomerization [43]. Further dissociation pathways are illustrated by Bafus [45] and Holtzclaw [47]: $C_2H_7O_3P^+$ (109 amu) looses formaldehyde to form $CH_4O_2P^+$ (79 amu), a loss of the methoxy radical leads to HPO^+ (48 amu), which becomes PO^+ (47 amu) after hydrogen dissociation. For $C_2H_7O_3P^+$ (110 am), an intial loss of the methoxy radical forms $CH_5O_2P^+$ (80 amu). Alternatively, the methyl radical is emitted to form $CH_6O_3P^+$ (95 amu) then followed by dissociation of formaldehyde resulting in $H_2O_2P^+$ (65 amu).

The cation yields as a function of proton energy in Figure 8 is almost constant over the displayed range between 1.55 MeV and 16 MeV. It shows an slight increase of the large fragments around 110 amu and decrease of smaller fragments around 79 amu at higher energies. A continuation of this trend towards the Bragg peak will be discussed in a follow-up paper.

4 Conclusion

In summary, relative fragmentation cross sections were measured for tetrahydrofuran, pyrimidine and trimethyl phosphate at the PTB Ion Accelerator Facility. Proton beam energies ranged from 0.3 MeV to 16 MeV, which is higher than Bragg peak energy for protons in tissue-equivalent material. Comparing with standard mass spectrometers working with about 70 eV electron impact ionization, proton impact was observed to induce stronger fragmentation with a higher ratio of small fragment cations.

In agreement with previous findings, the mass spectra can be interpreted such that the most severe fragmentation is found for the sugar part of the DNA, whose furanose ring is modeled by tetrahydrofuran. The tetrahydrofuran ring breaks in about 80% of all ionization events. A ring break in the sugar leads to a strand break in the DNA. For pyrimidine (corresponding to a base), the parent ion is more stable and has the highest abundance in the mass spectrum. Trimethyl phosphate (corresponding to the phosphate residue in the backbone) predominantly fragments by bond cleavage to one of the three methoxy-groups, which does not necessarily cause strand breaks. Within the limits of using isolated model molecules and a simple geometric relation to strand breaks, our data will be used in the GEANT4-DNA Monte Carlo simulation as a first step to relate fragmentation of DNA constituents to DNA damage.

Author contribution statement

H. Rabus conceived the experiment and supervised the work, A. Arndt designed and set up the instrument, B. Rudek, D. Bennett and M. Wang carried out the experiment, B. Rudek analysed the data and wrote the manuscript.

The authors like to thank O. Döhr and M. Hoffmann for operation of the PTB ion accelerators and A. Pausewang, W. Helms and V. Hahn for mechanical work. This work was carried out within the EMRP Joint Research Project BioQuaRT. The EMRP is jointly funded by the EMRP participating countries within EURAMET and the European Union.

References

1. B. Coupier, B. Farizon, M. Farizon, M.J. Gaillard, F. Gobet, N.V. De Castro Faria, G. Jalbert, S. Ouaskit, M. Carré, B. Gstir, G. Hanel, S. Denifl, L. Feketeova, P. Scheier, T.D. Märk, Eur. Phys. J. D **20**, 459 (2002)
2. J. de Vries, R. Hoekstra, R. Morgenstern, T. Schlathölter, Phys. Rev. Lett. **91**, 053401 (2003)
3. E. Surdutovich, O.I. Obolensky, E. Scifoni, I. Pshenichnov, I. Mishustin, A.V. Solov'yov, W. Greiner, Eur. Phys. J. D **51**, 63 (2009)
4. S. Martin, R. Brédy, A.R. Allouche, J. Bernard, A. Salmoun, B. Li, L. Chen, Phys. Rev. A **128**, 062513 (2008)
5. S. Bari, P. Sobocinski, J. Postma, F. Alvarado, R. Hoekstra, V. Bernigaud, B. Manil, J. Rangama, B. Huber, T. Schlathölter, J. Chem. Phys. (2008)
6. H. Rabus, H. Palmans, G. Hilgers, P. Sharpe, M. Pinto, C. Villagrasa, H. Nettelbeck, D. Moro, A. Pola, S. Pszona, P. Teles, Eur. Phys. J. Web Conf. **77**, 00021 (2014)
7. M.U. Bug, Ph.D. thesis, University of Wollongong, 2014
8. S. Ptasinska, S. Denifl, P. Scheier, T.D. Märk, J. Chem. Phys. **120**, 8505 (2004)
9. M.A.H. du Penhoat, P. López-Tarifa, K.K. Ghose, Y. Jeanvoine, M.P. Gaigeot, R. Vuilleumier, M.F. Politis, M.C. Bacchus-Montabonel, J. Mol. Mod. **20**, 2221 (2014)
10. S. Incerti, G. Baldacchino, M. Bernal, R. Capra, C. Champion, Z. Francis, P. Guèye, A. Mantero, B. Mascialino, P. Moretto, P. Nieminen, C. Villagrasa, C. Zacharatou, Int. J. Mod. Simul. Sci. Comput. **01**, 157 (2010)
11. R. Dörner, V. Mergel, O. Jagutzki, L. Spielberger, J. Ullrich, R. Moshammer, H. Schmidt-Böcking, Phys. Rep. **330**, 95 (2000)
12. D.A. Dahl, Int. J. Mass Spectrom. **200**, 3 (2000)
13. O. Hadjar, R. Hoekstra, R. Morgenstern, T. Schlathölter, Phys. Rev. A **63**, 1 (2001)
14. J.H. Gross, *Mass Spectrometry*, 2nd edn. (Springer, Berlin, Heidelberg, 2011)
15. S. Bari, F. Alvarado, J. Postma, P. Sobocinski, R. Hoekstra, T. Schlathölter, Eur. Phys. J. D **51**, 81 (2009)
16. J. De Vries, R. Hoekstra, R. Morgenstern, T. Schlathölter, Eur. Phys. J. D **24**, 161 (2003)
17. M.C. Bacchus-Montabonel, Eur. Phys. J. D **66**, 1 (2012)
18. F. Alvarado, S. Bari, R. Hoekstra, T. Schlathölter, J. Chem. Phys. **127**, 034301 (2007)
19. M.C. Bacchus-Montabonel, Eur. Phys. J. D **69**, 107 (2015)
20. U. Werner, K. Beckord, J. Becker, H. Lutz, Phys. Rev. Lett. **74**, 1962 (1995)
21. H.J. Brede, M. Cosack, G. Dietze, H. Gumpert, S. Guldbakke, R. Jahr, M. Kutscha, D. Schlegel-Bickmann, H. Schölermann, Nucl. Instrum. Methods **169**, 349 (1980)
22. R. Böttger, PTB Mitteilungen **112**, 1 (2002)
23. E.J. Gallegos, R.W. Kiser, J. Phys. Chem. **66**, 136 (1962)
24. J. Collin, G. Conde-Caprace, Int. J. Mass Spectrom. Ion Phys. **1**, 213 (1968)
25. M. Dampc, E. Szymanska, B. Mielewska, M. Zubek, J. Phys. B **44**, 055206 (2011)
26. H. Horai, M. Arita, S. Kanaya, Y. Nihei, T. Ikeda, K. Suwa, Y. Ojima, K. Tanaka, S. Tanaka, K. Aoshima, Y. Oda, Y. Kakazu, M. Kusano, T. Tohge, F. Matsuda, Y. Sawada, M.Y. Hirai, H. Nakanishi, K. Ikeda, N. Akimoto, T. Maoka, H. Takahashi, T. Ara, N. Sakurai, H. Suzuki, D. Shibata, S. Neumann, T. Iida, K. Tanaka, K. Funatsu, F. Matsuura, T. Soga, R. Taguchi, K. Saito, T. Nishioka, J. Mass Spectrom. **45**, 703 (2010)
27. P. Linstrom, W. Mallard, *NIST Chemistry WebBook, NIST Standard Reference Database Number 69* (National Institute of Standards and Technology, Gaithersburg MD, 20899, 2015)
28. U. Even, J. Jortner, D. Noy, N. Lavie, C. Cossart-Magos, J. Chem. Phys. **112**, 8068 (2000)
29. R.M. Young, M.A. Yandell, M. Niemeyer, D.M. Neumark, J. Chem. Phys. **133**, 1 (2010)

30. X. Ren, T. Pflüger, M. Weyland, W.Y. Baek, H. Rabus, J. Ullrich, A. Dorn, J. Chem. Phys. **141**, 134314 (2014)
31. A.A. Scala, E.W.G. Diau, Z.H. Kim, A.H. Zewail, J. Chem. Phys. **108**, 7933 (1998)
32. T.J. Wasowicz, B. Pranszke, J. Phys. Chem. A **119**, 581 (2015)
33. M. Fuss, A. Muñoz, J.C. Oller, F. Blanco, D. Almeida, P. Limão Vieira, T.P.D. Do, M.J. Brunger, G. García, Phys. Rev. A **80**, 3 (2009)
34. W. Wolff, H. Luna, L. Sigaud, A.C. Tavares, E.C. Montenegro, J. Chem. Phys. **140**, 064309 (2014)
35. M.C. Bacchus-Montabonel, J. Phys. Chem. A **118**, 6326 (2014)
36. F. Alvarado, S. Bari, R. Hoekstra, T. Schlathölter, Phys. Chem. Chem. Phys. **8**, 1922 (2006)
37. G. Vall-llosera, M. Coreno, P. Erman, M.A. Huels, K. Jakubowska, A. Kivimäki, E. Rachlew, M. Stankiewicz, Int. J. Mass Spectrom. **275**, 55 (2008)
38. I. Linert, M. Dampc, B. Mielewska, M. Zubek, Eur. Phys. J. D **66**, 20 (2012)
39. J.M. Rice, G.O. Dudek, M. Barber, J. Am. Chem. Soc. **87**, 4569 (1965)
40. F. Milani-Nejad, H.D. Stidham, Spectrochim. Acta Part A **31**, 1433 (1975)
41. P. Bolognesi, M.C. Castrovilli, P. O'Keeffe, A.R. Casavola, D. Catone, S. Turchini, L. Avaldi, Nucl. Instr. Meth. Phys. Res. B **279**, 118 (2012)
42. M. Schwell, H.W. Jochims, H. Baumgärtel, S. Leach, Chem. Phys. **353**, 145 (2008)
43. M.G.P. Homem, A. López-Castillo, M. Barbatti, L.F.S. Rosa, P. Iza, R.L. Cavasso-Filho, L.S. Farenzena, M.T. Lee, I. Iga, J. Chem. Phys. **137**, 184305 (2012)
44. Z. Deng, I. Bald, E. Illenberger, M.A. Huels, Phys. Rev. Lett. **95**, 1 (2005)
45. D.A. Bafus, E.J. Gallegos, R.W. Kiser, J. Phys. Chem. **70**, 2614 (1966)
46. E.J. Gallegos, R.W. Kiser, J. Am. Chem. Soc. **83**, 773 (1961)
47. J.R. Holtzclaw, J.R. Wyatt, J.E. Campana, Organic Mass Spectrom. **20**, 90 (1985)